



Published in final edited form as:

*Nat Biomed Eng.* 2020 March ; 4(3): 286–297. doi:10.1038/s41551-020-0527-8.

## High-resolution optoacoustic imaging of tissue responses to vascular-targeted therapies

Katja Haedicke<sup>1</sup>, Lilach Agemy<sup>2</sup>, Murad Omar<sup>3,4</sup>, Andrei Berezhnoi<sup>3,4</sup>, Sheryl Roberts<sup>5</sup>, Camilla Longo-Machado<sup>5</sup>, Magdalena Skubal<sup>1</sup>, Karan Nagar<sup>6</sup>, Hsiao-Ting Hsu<sup>5</sup>, Kwanghee Kim<sup>6</sup>, Thomas Reiner<sup>5,7</sup>, Jonathan Coleman<sup>6,8</sup>, Vasilis Ntziachristos<sup>3,4</sup>, Avigdor Scherz<sup>2</sup>, Jan Grimm<sup>1,5,7,9,\*</sup>

<sup>1</sup>Molecular Pharmacology Program, Memorial Sloan Kettering Cancer Center, 1275 York Ave, New York, NY 10065, USA.

<sup>2</sup>Department of Plant and Environmental Sciences, Weizmann Institute of Science, Herzl Street 234, Rehovot, Israel.

<sup>3</sup>Chair for Biological Imaging, Technical University Munich, Ismaninger Straße 22, 81675 Munich, Germany.

<sup>4</sup>Institute for Biological and Medical Imaging, Helmholtz Center Munich, Ingolstädter Landstraße 1, 85764 Neuherberg, Germany.

<sup>5</sup>Department of Radiology, Memorial Sloan Kettering Cancer Center, 1275 York Ave, New York, NY 10065, USA.

<sup>6</sup>Urology Service, Department of Surgery, Memorial Sloan Kettering Cancer Center, 1275 York Ave, New York, NY 10065, USA.

<sup>7</sup>Department of Radiology, Weill Cornell Medical College, 525 East 68<sup>th</sup> Street, New York, NY 10065, USA.

Reprints and permissions information is available at [www.nature.com/reprints](http://www.nature.com/reprints) Users may view, print, copy, and download text and data-mine the content in such documents, for the purposes of academic research, subject always to the full Conditions of use: [http://www.nature.com/authors/editorial\\_policies/license.html#terms](http://www.nature.com/authors/editorial_policies/license.html#terms)

\*Corresponding author: Jan Grimm, PhD, MD, [grimmj@mskcc.org](mailto:grimmj@mskcc.org).

### Author contributions

K.H. designed and performed all experiments, processed and analysed the RSOM data, evaluated histological sections and wrote the manuscript. L.A. performed the VTP experiments in CT26 tumours and provided practical input for study planning and performance. M.O. developed the RSOM system, supplied technical input and performed the dual-wavelength RSOM measurements and analysis. A.B. conducted the dual-wavelength RSOM experiments and analysis. S.R. conducted the craniotomy and performed the imaging of the mouse brain. K.N. performed the VTP experiments in bladder tumour models and supported RSOM imaging. H.T.H. performed the VTP experiments in bladder tumour models and supported histological analysis. K.K. provided conceptual input and designed the experiments in bladder tumour models. T.R. provided input for the design of the brain experiments. J.C. provided input and designed the VTP experiments. V.N. provided technical input for RSOM imaging and supervised the dual-wavelength measurements. A.S. supervised the VTP experiments, provided conceptual input and designed the experiments. J.G. supervised the study, provided input for all experiments and the study concept, and edited the paper.

### Data availability

The authors declare that all data from this study are available in the paper and its Supplementary Information. Raw data for the individual measurements are available on reasonable request.

### Competing interests

V.N. is a shareholder in iThera Medical GmbH in Munich, Germany, which produces a commercial version of the monospectral RSOM (not used in this study). A.S. is an inventor of Padeliporfin and has a financial interest from licensing fees.

**Supplementary information** is available for this paper at <https://doi.org/10.1038/s41551-01X-XXXX-X>.

**Publisher's note:** Springer Nature remains neutral with regard to jurisdictional claims in published maps and institutional affiliations.

<sup>8</sup>Department of Urology, Weill Cornell Medical College, 525 East 68<sup>th</sup> Street, New York, NY 10065, USA.

<sup>9</sup>Pharmacology Program, Weill Cornell Medical College, 1300 York Avenue, New York, NY 10021, USA.

## Abstract

The monitoring of vascular-targeted therapies via magnetic resonance imaging, computed tomography or ultrasound is limited by their insufficient spatial resolution. By taking advantage of the intrinsic optical properties of haemoglobin, here we show that raster-scanning optoacoustic mesoscopy (RSOM) provides high-resolution images of the tumour vasculature and of the surrounding tissue, and that the detection of a wide range of ultrasound bandwidths enables the distinction of vessels of differing size, allowing for detailed insights into vascular responses to vascular-targeted therapy. By using RSOM to examine the responses to vascular-targeted photodynamic therapy in mice with subcutaneous xenografts, we observed a significant and immediate occlusion of the tumour vessels, followed by haemorrhage within the tissue and the eventual collapse of the entire vasculature. By using dual-wavelength RSOM, which distinguishes oxyhaemoglobin from deoxyhaemoglobin, we observed an increase in oxygenation of the entire tumour volume immediately after the application of the therapy, and a second wave of oxygen reperfusion approximately 24 h thereafter. We also show that RSOM allows for the quantification of differences in neo-angiogenesis that predict treatment efficacy.

---

With the intent of depriving cancer cells of nutrients and oxygen and reducing metastasis, many cancer therapies have been developed to either arrest existing tumour perfusion (anti-vascular) or prevent neovascularization (anti-angiogenic). While anti-angiogenic drugs such as bevacizumab have shown some promise, their efficacy is limited by the development of therapeutic resistance, as well as ensuing tumour hypoxia and subsequent impaired drug delivery, which might explain the disappointing overall survival after anti-angiogenic therapy<sup>1</sup>. These unexpected effects highlight the need for a means of monitoring the effects of anti-vascular and anti-angiogenic therapy in vivo over time.

Until recently, the therapeutic response of tumour vessels could only be examined in either a small area or at low resolution. Available methods include intravital microscopy, an invasive procedure with a small field of view; real-time laser speckle imaging, which is limited to a small tumour volume; or low-resolution non-invasive modalities such as blood oxygenation level-dependent (BOLD) magnetic resonance imaging (MRI), diffuse optical tomography to follow e.g. chemotherapy response in breast cancer; bioluminescence imaging of luciferase-transfected tumours, and ultrasound imaging of anti-vascular therapy-induced tumour necrosis<sup>2-7</sup>. More recently, anti-vascular therapeutic effects have been monitored using conventional multispectral optoacoustic tomography (MSOT), a method that offers views of the entire tumour but also only at low resolution that does not allow to depict vascular structures<sup>8</sup>. In addition, a 640 nm photoacoustic scanner was used to observe the pharmacodynamic response of a chemotherapeutic agent, however, this observation also only showed longitudinal changes in low resolution, detecting only bigger vessels surrounding the tumour tissue, and did not use broad ultrasound bandwidth or dual-spectral

imaging to resolve different states of oxygenation<sup>9</sup>. Therefore, none of these modalities enables analysis of the vascular bed with simultaneous quantification of changes in the level of oxygenation at such high resolution as presented here when using the dual-wavelength modality. Importantly, none of these modalities provided predictive parameters for tumour response or allowed for the detection of early or late biological effects.

The imaging modality of raster-scanning optoacoustic mesoscopy (RSOM) in contrast provides non-invasive, high-resolution images of the entire tumour vasculature and surrounding tissue vessels. While MSOT uses a 5 MHz tomographic approach for signal detection, where the whole body of the animal can be imaged with a multispectral 10 Hz laser at resolutions of about 160  $\mu\text{m}$ <sup>10</sup>, RSOM uses a raster-scanning approach with fast nanosecond-pulsed (up to 2 kHz) laser excitation of tissues and tumours and a 50 MHz single element transducer. The highly pulsed laser and high frequency detector allow for high-resolution images. Absorption of the transient light energy by tissue chromophores, such as haemoglobin contained within blood vessels, generates ultrasound signals through short thermoelastic expansion of the excited molecules<sup>11</sup>. Ultra-wide bandwidth detectors and narrow laser pulses allow for the generation of high-resolution optical absorption images, revealing sub-millimetre fine vascular structures up to several millimetres in depth<sup>12</sup>.

The first application of RSOM has been to resolve the vasculature of a melanoma tumour and the vascular bed surrounding the tumour tissue *in vivo* over time with up to 5  $\mu\text{m}$  axial and 20  $\mu\text{m}$  lateral resolution<sup>13</sup>, though melanin in the tumour limited the signal penetration. RSOM has also been used to image the whole body of zebrafish using a 360° multi-orientation approach<sup>14</sup>. In humans, RSOM has been demonstrated to distinguish individual layers of skin and to depict a benign nevus<sup>15,16</sup>, to reveal simple hyperthermia effects<sup>17</sup>, and to detect pathophysiological biomarkers of psoriasis and inflammation<sup>12</sup>. Additionally, dual-spectral RSOM imaging has been shown to discern melanin and blood oxygenation in normal human skin<sup>18</sup>. However, RSOM has only yet been used to generate static snapshots of benign events and has never been used in any oncology studies or to monitor dynamic changes.

Herein, we explored RSOM and dual-wavelength RSOM as a non-invasive and high-resolution imaging tool to characterize tumour vessels and to quantify the dynamic response to an anti-vascular cancer therapy at the mesoscopic level in several mouse models of cancer. Particularly, we aimed to demonstrate the ability of RSOM to visualize the formation of blood vessels in high resolution and to evaluate response of tumour vessels to pharmacologic stimuli over only a few minutes. Finally, we monitored the outcome of vascular-targeted photodynamic therapy (VTP) with Padeliporfin (Tookad®-soluble)<sup>19,20</sup>, a palladium-bacteriochlorophyll derivative photosensitizer that was recently clinically approved for non-thermal ablation of early-stage low-risk prostate cancer following clinical trials in Europe<sup>21–23</sup>. Treatment is achieved by tail vein infusion of Padeliporfin, after which the tumour area is selectively illuminated with a 753-nm laser, locally exciting Padeliporfin in the bloodstream<sup>19</sup>. This induces the generation of oxygen radicals<sup>24</sup> from blood-borne oxygen, leading to irreversible vascular occlusion, followed by tumour cell death and ultimately ablation of the tumour. One of the major advantages of Padeliporfin is its fast

clearance from the bloodstream, reducing unwanted side effects of skin photosensitivity or accumulation in other organs<sup>19</sup>.

We examined the correlation between the vascular response and the therapeutic efficacy of VTP using Padeliporfin. We evaluated both immediate short-term changes within single blood vessels and long-term effects and alterations across the whole tumour vascular bed and its surrounding tissue over several days. Lastly, we aimed to identify RSOM-derived parameters that could be used to predict treatment response and shed light on VTP's mechanism of action. The integration of a second pulsed laser into the RSOM system allowed us to evaluate oxy- and deoxyhaemoglobin, providing the opportunity to image oxygen distribution within and around the tumour after therapy.

## Results

### RSOM imaging of tumour vascular growth and brain vasculature.

We first evaluated RSOM as a means of monitoring the tumour vascular bed during the growth of subcutaneous CT26 colon carcinoma tumours. Separating ultrasound signals into lower (5–25 MHz) and higher (25–80 MHz) frequencies revealed a complex network of tortuous tumour vessels, in which larger vessels (coded as red) branch out into smaller vessels (coded as green) (Fig. 1b). Merging both sub-bands revealed an overlap of high and low frequencies (orange to yellow colour in the images), indicating that several vessels emit in both frequency bands and are of intermediate size, which was also seen by scanning through different depths of the tumour (Fig. 1c). Reconstructing a 3D image of the tumour revealed the three-dimensional vascular network within the tumour in detail (Fig. 1c, bottom, Suppl. Movie 1). Sequential RSOM images of CT26 tumour growth showed that an intricate vascular network of smaller vessels developed as early as 3 days after implantation (Fig. 1d). At around day 8, tumour vessels appeared more mature, as the proportion of smaller vessels decreased, and larger vessels formed. At day 17 after tumour implantation, a branched and chaotic vascular system became predominant. These analyses demonstrate that RSOM allows visualization of changes in tumour vasculature over time at vessel-level resolution. Depth analysis revealed that vessels up to ~2.5 mm could be visualized under good conditions in a subcutaneous tumour, i.e. smaller tumours can be scanned in their entirety.

RSOM was then applied to image a mouse brain through the intact skull as well as the exposed brain after removing the skullcap (Fig. 1e). Mainly bigger vessels were visible through the enclosed skull while very fine structures and smaller vessels became visible in the exposed brain, both, in the dorsal as well as the lateral view of the brain. The main artery in the middle of the brain and smaller branches could be clearly detected. The lateral view showed the curvature of the brain and deeper blood vessels.

So far, *ex vivo* histological methods are used extensively to interrogate blood vasculature. Although a powerful technique, it requires multiple laborious steps to clear the tissue to even see vessels, including cryo-sectioning, staining, clearing and scanning of multiple consecutive slides. Yet, RSOM is advantageous over histology in several ways: RSOM allows for repeated *in vivo* tracking of tumour vasculature over in the same animal; it can

cover a wider imaging area ( $>4\times$ ) at higher depths without the need of image stitching. Artefacts from tissue fixing, cutting and staining are also not an issue. Multiplexing of frequency bands allows small and larger vessels to be distinguishable from each other and adds greater accuracy to the way we can use it to observe and track vessels of interests.

### Visualizing epinephrine- and endothelin-induced vasoconstriction.

As a first step, intensity profiles were taken from blood vessels in a CT26 tumour to proof the detectable vessel diameter (half-maximum width of the profile) in RSOM (Suppl. Fig. 1a–b). From the sagittal view, vessels with 20  $\mu\text{m}$  in diameter could be detected. In axial view, vessels with a diameter of 40  $\mu\text{m}$  are visible. The different resolution comes from the detector design and having only one transducer element scanning from above along the skin surface.

To demonstrate that RSOM can identify small, early changes within a tumour's vascular network, we imaged pharmacologic vasoconstriction of individual vessels. At 1 min after injection of epinephrine, a reduction in diameter of individual vessels within CT26 tumours was clearly discernible on enlarged MIP images. The ultrasound frequency emitted by several vessels (Fig. 2a) changed from low (red) to high (green), consistent with a decrease in vessel width. At 5 and 10 min after injection, tumour vessels began to dilate, as indicated by a return to a lower frequency signal (yellow/red). The same observations were made after injection of endothelin-1 (Fig. 2b): clear vasoconstriction at 1 min after injection, apparent as emission of higher frequencies (green), and vasodilation (return to lower frequencies) within 5 min to 10 min. (Fig. 2b, **inserts**). At 10 min after vasoconstriction using either agent, several new vessels appeared.

Quantification of the diameter of single tumour vessels in several animals over time confirmed an almost 50% decrease in vessel size at 1 min following injection of either epinephrine or endothelin-1, and that vessels returned to baseline diameter by 10 min post-injection (Fig. 2c–d). Interestingly, normal vessels of the surrounding skin reacted differently, failing to contract at all as visualized in RSOM MIP images (Suppl. Fig. 2a–b). A quantification of representative skin vessel diameters in several animals confirmed this observation; vessel diameters remained nearly unchanged over time after injection of either vasoconstrictor agent (Suppl. Fig. 2c–d), which is probably species-specific. The ability of RSOM to reveal changes at the level of individual vessels over time demonstrates this modality's high sensitivity.

### Monitoring the efficacy of VTP in CT26 tumours using RSOM.

VTP was performed by infusing the photosensitizer Padeliporfin intravenously, followed by immediate laser illumination of the tumour, and the treatment effect was monitored over the next hour by RSOM imaging (Fig. 3a). Single-layer images through varying depths of a small (diameter  $<6$  mm), low vascularized CT26 tumour revealed distinct vascular events (Fig. 3b). In superficial tumour vessels (at 350  $\mu\text{m}$  depth from the skin surface), VTP induced intravascular clotting as indicated by denser optoacoustic signals. Vessels deeper inside the tumour (at 570  $\mu\text{m}$  depth from the skin surface), clearly visible before VTP, occluded and disappeared within 10 min after illumination. As vessels lost integrity,

haemorrhage became visible as an irregular red spot inside the tumour, not confined to vascular architecture. In addition, clotting of smaller vessels was detected as more intense signals in the vascular pattern, especially at the tumour rim, reflecting the higher density of haemoglobin within blood clots. RSOM revealed blockage and destruction of the larger tumour-feeding skin vessels over time, visible as a decrease in signal. Quantitative analysis of the relative haemoglobin signal in RSOM images over time confirmed these observations (Fig. 3c).

Following VTP treatment in larger (diameter >6 mm), more vascularized CT26 tumours, RSOM clearly showed vascular constriction followed by destruction of several blood vessels. Here, larger tumour vessels were occluded at 5 min after VTP (Fig. 4a). Single vessels could be followed throughout the progress of VTP effects. At 1 h, occlusion and disappearance of small vessels was pronounced and accompanied by slight haemorrhage, appearing as red spots within the RSOM images. Quantification of relative haemoglobin levels over time after VTP showed that signal decreased within 5 min after VTP in both low- and high-frequency bands, reflecting destruction of both larger and smaller vessels (Fig. 4b, left). The number of vessel fragments increased due to vessel breakage (Fig. 4b, right). Histological analysis corroborated these observations (Suppl. Fig. 3), revealing, at 1 h after VTP, damage to tumour tissue (H&E), massive destruction of tumour blood vessels (CD31), and apoptotic/necrotic cells (TUNEL), in contrast to untreated control tumours, in which tumour tissue remained intact, with many vessels and no obvious dead cells. These analyses demonstrate the suitability of RSOM imaging for quantitative monitoring of rapid changes in tumour vasculature in real time.

### Long-term monitoring of the VTP efficacy using RSOM.

Next, we used RSOM to monitor larger, more vascularized tumours over 5 days after therapy. The tumours demonstrated visible changes following VTP, including slight redness and swelling at 24 h, eschar, oedema, and necrotic tissue at 48 h after VTP, which began to shrink after 5 days (Fig. 4c). RSOM MIP images demonstrated destruction of individual vessels at 1 h after VTP, accompanied by some haemorrhage (Fig. 4d, Suppl. Fig. 4). Between 1 and 24 h post-VTP, the initially non-vascularized tumour tissue was perfused, and between 18 and 24 h, vessel appearance normalized. Vessels not visible before VTP expanded and became perfused with blood, revealing a fine-structured and interconnected vascular network throughout the tumour. This opening of alternative blood sources probably reflects the “intermittent blood flow” phenomenon<sup>3,25</sup> and underscores the need to continue illumination until the entire tumour vasculature collapses. However, this effect was short-lived. Beginning at 48 h and even more visible at 5 days after VTP, the complete tumour vascular network collapsed, and defined vessel structures resolved. Hereby, the dusky tissue appearing on the tumour after VTP, might absorb some of the laser light, slightly decreasing the imaging depth but still allowing the visualization of vascular changes such as strong necrosis and oedema. Quantification of RSOM images revealed that both the vascular area and the number of vascular fragments initially increased due to vascular breakage, returned to baseline between 24 and 48 h due to reperfusion and normalization, then continued to decline up to 5 days after VTP as a result of total vascular collapse (Fig. 4e). At 5 days after VTP, the signal from the treated necrotic tumour became homogenous, reflecting massive

haemorrhage (i.e. even vessel fragments were no longer discernible). Haemoglobin signal in both low and high frequency channels followed a similar pattern. At day 5 the RSOM images showed no perfusion. In agreement with RSOM findings, histological examination revealed 90–100% tumour tissue necrosis at 24 h (H&E), as well as deterioration of blood vessels (CD31) and a large number of apoptotic/necrotic cells (TUNEL) (Suppl. Fig. 3). At day 5, no vessels were apparent by CD31 staining, and no viable tissue was detectable by H&E in the tumour area.

### **Dual-wavelength RSOM of blood oxygenation changes after VTP.**

To obtain dual-wavelength RSOM images, a second nanosecond pulsed laser with a wavelength of 515 nm was added to the system. This enabled together with the 532 nm laser the discrimination of oxy- from deoxyhaemoglobin (Fig. 5a). The absorbance of oxyhaemoglobin is lower than that of deoxyhaemoglobin at 515 nm and vice versa at 532 nm, so the ratio of the signals generated at those two wavelengths can be used to calculate relative levels of oxygenated haemoglobin within the tissue, visualized as a colour gradient.

This dual-laser system identified a clear decrease in oxygenation within the tumour at 1 h after VTP (relative to pre-treatment baseline), as presented in 3D surface plots (Fig. 5b). The same effect was visible in the RSOM MIP images of the same tumour (Fig. 5c). A more detailed analysis revealed a temporary increase in oxygenated haemoglobin throughout the tumour 5 minutes after VTP (Fig. 6a), indicating rapid reperfusion. The oxygenation level then dropped, shown as a reduction of the red oxygenated area and an expansion of the blue deoxygenated area. Quantification of these images demonstrated a shift towards lower oxygenation values (into the blue end of the scale), from a mean value of 35,089 AU before VTP to 24,618 AU at 1 h post-treatment (Fig. 5d). At 24 h post-VTP, tumour vessel oxygenation almost ceased (Fig. 6a), corroborated by clotting and necrosis (homogenous signal) seen on the 532 nm vascularization images (Fig. 6a, lower panels). Quantification of relative oxygenation confirmed the patterns seen in gradient images; an increase in oxygenation at 5 min after VTP, followed by a large decrease up to 24 h (Fig. 6b). Thus, quantitative analysis of oxygenation levels enabled by dual-wavelength RSOM allows examination of functional effects of anti-vascular therapies in real time.

### **RSOM imaging of varying degrees of tumour control by VTP.**

We next sought to evaluate RSOM as a tool to predict treatment response. Based on their distinct cure rates at 15 days post-VTP, we chose models of bladder cancer in which either UMUC3 or 5637 patient-derived cells were xenografted into mice; UMUC3 tumours were less effectively treated by Padeliporfin VTP than 5637 tumours. RSOM images of UMUC3 tumours showed more extensive neo-angiogenesis compared with 5637 tumours (Fig. 7a). Interestingly, as early as 1 h until 24 h after treatment, ischemic reperfusion of initially non-vascularized tumour tissue was apparent in 5637 tumours (similar to CT26 tumours; Fig. 4d), but minimal in UMUC3 tumours, in which mostly larger vessels deteriorated by 24 h. At 3 days after treatment, the vasculature of 5637 tumours completely collapsed, and the periphery of the tumour was vessel-free, whereas UMUC3 tumours exhibited a necrotic tumour centre with regrowth of small new vessels at the outer edges. While 5637 tumours lost all remaining vessels, UMUC3 tumours grew a new vascular network. Tumour volume

measurements in these two models confirmed these observations (Fig. 7b); 5637 tumours shrank, while UMUC3 tumours increased in volume after VTP. These findings were further substantiated by white light photographs (Suppl. Fig. 5), showing complete tumour necrosis and a scab after VTP in 5637 tumour-bearing mice, and central necrosis with extensive neo-angiogenesis and regrowth at the tumour rim at day 3, resulting in a larger tumour at day 14 post-VTP, in UMUC3 tumours.

Quantification of RSOM MIP images revealed obvious differences in relative haemoglobin signal, vascular area, and vessel fragments that was consistent with treatment effect (Fig. 7c). While the relative haemoglobin signal remained fairly stable in both models up to 24 h after VTP, with only a slight increase in the lower frequency channel in UMUC3 tumours due to haemorrhage, a decrease in signal was observed after 3 days only in 5637 tumours (Fig. 7c, left). The haemoglobin signal remained low in 5637 tumours, with a minimal increase in the lower frequency channel at day 14 due to necrosis and scarring. The overall vascular area in the 5637 tumours first increased slightly up to 24 h after VTP and decreased starting at 3 days (Fig. 7c, middle). In comparison, the vascular area in UMUC3 tumours increased slightly up to day 7 after treatment, then rose at day 14 due to regrowth of new vessels. The number of vessel fragments increased in the 5637 tumours immediately after therapy due to vessel destruction and continued to decrease thereafter (Fig. 7c, right), while in UMUC3 tumours it increased steadily due to the regrowth of new and more vessels, especially at 14 days after VTP. The ratio of high-frequency signal (small vessels) to the vascular area was much higher in 5637 versus UMUC3 tumours from day 3 on (Fig. 7d); at a time when the change in tumour volume was not yet apparent. Histopathology using H&E and CD31 staining corroborated these results (Suppl. Fig. 6), showing destruction of tissue and loss of vessels in 5637 tumours, and regrowth of only slightly deteriorated tumour tissue and tumour blood vessels in UMUC3 tumours. These findings suggest that RSOM may enable early differentiation of varying treatment effects of VTP and possibly other anti-vascular and anti-angiogenic treatments.

## Discussion

We have described the application of RSOM for detailed imaging of temporal changes in tumour vascularization and oxygenation levels during and after vascular-targeted therapy. Together, our results demonstrate the ability of RSOM to unveil important aspects of the tumour microenvironment's response to vascular-targeted treatments, clarify their mechanisms of action, and improve treatment approaches. This imaging tool allows for the non-invasive study of morphological and functional aspects of vessels at much deeper levels than optical microscopy and with high resolution, improving significantly over existent non-invasive approaches to image the vascular bed in unprecedented detail. Furthermore, compared to elaborate histology, temporal changes can be observed in the same animal.

We first evaluated the ability of RSOM to capture changes in tumour vascular morphology coincident with tumour growth over 17 days. RSOM images revealed an elaborate vascular network in CT26 tumours, which changed appearance as a function of time, revealing a progressive recession of smaller vessels with tumour growth and the development of a chaotic vascular system. RSOM therefore allows non-invasive, high-resolution imaging of



tumour neo-angiogenesis, an advance over previous techniques for imaging of tumour vascular growth, which were either low-resolution and non-invasive or high-resolution and invasive<sup>3,8</sup>. Our study reveals vascular details within a tumour itself, as the prior investigation was limited by the presence of strongly absorbing melanin within the tumour (a melanoma), and therefore mainly captured the vascular bed surrounding the tumour<sup>13</sup>, unable to penetrate into the tumour itself.

RSOM allows following relatively short temporal changes in the vascular bed of tumours and normal tissue as demonstrated here using pharmacologic manipulation with epinephrine or endothelin-1 administration. RSOM consistently identified immediate diameter changes in individual CT26 tumour vessels, confirming their functional ability to respond to external stimuli. These findings demonstrate the high sensitivity of RSOM in capturing even minor alterations within a complex vascular network non-invasively. While the exact biological mechanism behind the intriguing responsiveness of tumour vessels to vasoconstrictors and non-responsiveness of those in the surrounding skin requires further investigation, we surmise that it may result from recruitment of smooth muscle cells into the tumour, lowering their numbers in adjacent areas. Previous studies showed that pericytes are present in most tumour vessels, but show multiple abnormalities compared to those associated with normal capillaries, such as overexpression of alpha-smooth muscle actin<sup>26</sup>.

The ability of RSOM to follow changes in vessel diameter, as demonstrated here, provides an interesting opportunity to monitor vascular normalization in response to therapy. Such normalization is necessary to support delivery of chemotherapeutics and radiotherapeutics to certain tumour types<sup>27,28</sup>. This effect has previously been imaged at very low resolution using daily MRI or PET<sup>29,30</sup>. The colour-coding system presented here, in which changes in vascular diameter are represented as changes in colour, allows real-time monitoring of such changes. The benefit of RSOM as a tool to aid the design and improvement of new and established treatments is also demonstrated by its ability to detect the immediate opening of alternative blood vessels. Both chemo- and radiotherapy are most effective in homogeneously well vascularized tumours, which deliver the drug or oxygen radical throughout the tumour. Hence, the intermitted blood flow, whereby different tumour domains may undergo perfusion at different time points, limits treatment to the perfused domains only. Monitoring changes in the perfusion of different tumour domains may enable better targeted pulsed radiolysis and may account for the observed advantage of intermittently applied chemotherapies.

The ability of RSOM to provide a detailed picture of vascular events and resulting changes in tissue oxygenation levels is demonstrated by our monitoring of VTP efficacy using the clinically approved photosensitizer Padeliporfin in the CT26 tumour model. Changes in tumour functional parameters have recently been observed in tumours in response to Padeliporfin treatment using MSOT, which offers views of the entire tumour but only at low resolution<sup>8</sup>. Herein, we applied RSOM to elucidate responses at a resolution of a few micrometres at both short- and long-term intervals on the individual vessel and whole-tumour level. This had previously only been possible invasively by intravital fluorescence microscopy, or, with certain limitations, using real-time laser speckle imaging with a dorsal window chamber in mice, or by basic low resolution modalities<sup>3,4,19,31,32</sup>. However, none of

these modalities enabled simultaneous quantification of changes in the tissue level of oxygenation at a high enough resolution to visualize individual vessels, as presented here, showing the utility of RSOM in resolving the action mechanism of tumour treatment that involves vascular targeting and also whole tissue response. While previously published studies focused on the vascular events involved in tumour destruction, our study was even able to shed some highlight onto the action mechanism of this tumour treatment. Here, the higher temporal and spatial resolutions of RSOM combined with multispectral analysis and wide bandwidth compared to other methods allowed to observe a transient oxygen reperfusion in the first few minutes post treatment. Notably, oxygen reperfusion is widely believed to be the major contributor to organ collapse in sepsis or stroke, all caused by ischemia/reperfusion injury rather than the ischemia alone. Moreover, the self-propagation of radicals into the tumour core necessary for the VTP requires continuous provision of oxygen radicals enabled through the release of oxygen from haemoglobin into the tumour stroma, some of which could at later timepoints arise from haemorrhage into the tissues as reservoir for oxygenated haemoglobin. Indeed, the observed temporal increase in oxygenation throughout the entire tumour tissue at 5 min post VTP and the slow decay observed long after the completion of vascular occlusion indicate that VTP leads to oxygen reperfusion outside vessels that is sustained for several hours, while the level of oxygen in the vessels drops. Combined with the observed overall ischemia, these findings suggest that VTP induces ischemia reperfusion injury. While the vascular events are consistent with previous macroscopic observations performed by MSOT and other photoacoustic imaging systems<sup>8,33</sup>, the observed oxygen reperfusion and predictive parameters provide an important insight into VTP's mechanism of action. Furthermore, tumour oxygenation has been identified as a prognostic indicator of treatment outcome in previous studies<sup>33,34</sup>, pointing out the potential impact of such physiologic parameter monitoring for personalized treatments. A limitation of the previous studies, however, is the poor spatial resolution of the images as mentioned before. Our current approach with RSOM represents a significant advantage in technology by providing a means for high-resolution imaging of tumour blood vessels and oxygenation in a way that could inform the delivery of light for treatment by mapping not only oxygen distribution. RSOM could consequently be used to guide the delivery of adjuvant treatments to areas at high risk for recurrence.

To determine whether quantitative parameters derived from RSOM image features correlate with treatment success, we compared several changes in tumour vasculature following VTP in tumours grown from different cell lines (UMUC3 and 5637, both bladder carcinoma), which showed distinct cure rates upon VTP (possibly due to differences in size and from increased angiogenesis). The profound differences in vascular changes between these tumour types indicate that RSOM parameters of vascular response may be useful for predicting treatment success before changes in tumour volume or tumour growth become apparent. Furthermore, specific differences between the effects in these tumours may provide insights into the biological mechanisms of response. For example, the primary vascular response in all tumour types appears initially similar, including breakdown (occlusion) of feeding arteries and draining veins, haemorrhage, and clot formation. However, re-growing tumours show evidence of recruitment of new vessels from the periphery, whereas non-re-growing tumours do not. Thus, the vascular area of the re-

growing tumours (including immediately adjacent tissue) is significantly larger, which could be used as an early indicator of regrowth. These findings demonstrate that RSOM provides a useful means to quantitatively examine the effects of modern vascular-targeted therapies, providing details regarding potential biologic mechanisms that can be further investigated to improve therapeutic efficacy. In the future, and with the inclusion of several wavelengths, the applications of RSOM could potentially be extended beyond imaging only blood vessels but also genetically modified tumour cells or other tissue processes as outlined with other, lower resolution optoacoustic scanners<sup>35</sup>. Furthermore, it might also be feasible in the future to use RSOM for endoscopic imaging as was shown as a proof of concept in ex vivo swine phantoms<sup>36</sup>, widening the applications especially for orthotopic tumours. Also, our brain imaging data suggest the future use of RSOM for imaging orthotopic tumours in several organs, especially in preclinical research, expanding the potential of RSOM significantly.

One of the limitations of RSOM is the limited penetration depth, inherent to all high-resolution ultrasound detectors. However, in the context of our study this was not a significant limitation since we could proof that imaging of the rather surface-near tumour vessels is sufficient to predict treatment outcome for responding and non-responding tumours. Furthermore, the regrow of vessels hereby happened rather starting from the surrounding tumour tissue and not from the tumour core, which could clearly be depicted using RSOM. In addition, histology images, even from deeper inside the tumours, confirmed the features seen in the RSOM images.

In conclusion, we confirmed RSOM as a method to observe vascularity during tumour development as well as to visualize critical changes in response to therapy. RSOM allows detailed, quantitative observation of morphological (vascularization) and physiological (oxygenation) features of tumour vascular dynamics that may inform the evaluation and development of new therapies, and could be translated to a broad spectrum of other applications.

## Methods

### In vitro cell culture.

Mouse colon carcinoma cells (CT26) were cultivated in RPMI 1640 media (D-Glucose concentration 2000 mg/L, cat. # 10-040, Corning) supplemented with 2 mM L-glutamine (cat. # 25030081, Thermo Fisher Scientific), 1 mM sodium pyruvate (cat. # 25-000, Corning), 1% penicillin/streptomycin solution (cat. # 30-002, Corning) and 10% foetal bovine serum (cat. # 100-106, GeminiBio). Human urinary bladder grade II carcinoma cells (5637) from ATCC were cultured in RPMI 1640 media with 10% foetal bovine serum, 2 mM L-glutamine and 1% penicillin streptomycin solution. Human urinary bladder transitional cell carcinoma cells (UMUC3) from ATCC were grown in MEM media (D-Glucose concentration 1000 mg/L, cat. # 10-010, Corning) with the same supplements as for 5637 cells. All cell lines were incubated at 37 °C in a 95% humidified atmosphere with 5% CO<sub>2</sub>.

### Animal models and tumour implantation.

CT26 tumours were implanted into female BALB/c mice (Taconic, 6–8 weeks old) by subcutaneous injection of  $1 \times 10^6$  CT26 cells in 100  $\mu$ L of 1:1 Matrigel (cat. # 354234, Corning) and PBS (cat. # 46–013, Corning) into the upper region of the thigh. 5637 and UMUC3 tumours were grafted into male NSG mice (NOD.Cg-Prkdc<sup>scid</sup> Il2rg<sup>tm1Wjl</sup>/SzJ, Jackson Laboratory, 6–8 weeks old) by injecting  $10 \times 10^6$  or  $3 \times 10^6$  cells, respectively, subcutaneously in 100  $\mu$ L of 1:1 Matrigel and media into the right flank. Tumour growth was monitored over time; imaging was performed, and therapy delivered under 2% isoflurane inhalation anaesthesia (Forane Isoflurane, cat. # NDC10019–360-60, Baxter) when implants reached sufficient size of at least 6 mm diameter (for CT26 tumours, approximately 14 days after implantation; for 5637, 33 days; and for UMUC3, 18 days). All mice were shaved with depilatory cream (Hair Removal Lotion, Nair) before RSOM imaging to prevent light absorption and reduced image quality due to hair. During shaving and therapy application, mice were placed on a warm cushion. Temperature was not monitored during the imaging sessions. All animal procedures were approved by the Institutional Animal Care and Use Committee (IACUC) and followed institutional and NIH guidelines.

### Raster-scanning optoacoustic mesoscopy (RSOM).

Optoacoustic images were generated using a prototype scanner and a MatLab based software developed at the Helmholtz Centre in Munich as described previously<sup>13,37</sup>. Specific RSOM scanner parameters are provided in Supplementary Table 1. In short, the anesthetized mouse was placed on a bed into a warmed water bath with the tumour region under and the head above the water level (Figure 1a). The tumour was stabilized using thin plastic wrap to suppress breathing motion artefacts. Three laser fibres, together with the 50 MHz spherically focused ultrasound detector, were placed just above the tumour, and the designated area was scanned in a raster fashion, with 20  $\mu$ m steps. The scan time for a field of view of  $6 \times 6$  mm was approximately 1.5 min, for a larger field of view of  $10 \times 10$  mm about 4 min. During scanning, the tissue was illuminated using a nanosecond pulsed 532 nm laser, which excites haemoglobin. The generated ultrasound signals were detected at a bandwidth of 5 to 80 MHz. Signals were subsequently amplified and digitized. During image reconstruction, 532 nm laser induced signals were separated into lower (5–25 MHz, colour-coded in red) and higher (25–80 MHz, colour-coded in green) frequencies to distinguish larger (48–240  $\mu$ m diameter) and smaller (15–48  $\mu$ m diameter) vessels<sup>13,37</sup>, respectively. This bandwidth separation was done for all images in the exact same way by using the same frequency ranges, meaning that larger (red encoded) and smaller (green encoded) vessels represent the same size range throughout the whole study, also over time after treatment. For clarity of the figures the scale bar is shown in Figure 1, this bar applies to all images unless specified otherwise. With the formula  $f_c \sim 0.8c/d$ , with  $f_c$  being the centre frequency,  $c$  representing the speed of sound with 1500 m/sec and  $d$  the diameter of the vessel, the dependency of detected frequency from vessel size can be calculated<sup>38</sup>. Images were processed using the Hilbert transform (assuming a speed of sound of 1540 m/s) along the depth as well as a Median and Wiener filter. Unless otherwise specified, images represent the maximum intensity projection (MIP) of the 3D volume, seen from above the tumour, as an RGB image (scaled always from 0 to 255) merging the low (red) and high (green) frequencies. Structures

emitting frequencies in both frequency bands appear in orange to yellow colour in the images. Specific features of the RSOM images and its biological interpretation are listed in Table 1.

For dual-wavelength RSOM to discriminate oxy- and deoxyhaemoglobin, a second laser with a wavelength of 515 nm was added. Images were acquired for both wavelengths simultaneously and the corresponding data for each wavelength separated before reconstruction. The detected ultrasound bandwidth for this approach was 10 to 100 MHz. The ratio of the signals at 532 nm to signals at 515 nm was used to calculate the relative gradient of oxygenated haemoglobin.

### **RSOM imaging of CT26 tumour vascular growth over time.**

CT26 tumours were implanted as described before. Prior to imaging, the tumour area and its immediate surroundings were shaved to reduce imaging artefacts. The tumour area was imaged by RSOM starting immediately after tumour implantation (day 0), and at days 3, 8, 13, and 17 after inoculation to assess vascular changes accompanying tumour growth.

### **Craniotomy and brain imaging.**

Under isoflurane anaesthesia, the mouse was placed in a stereotaxic frame, over a surgery warmer bed and the head firmly secured with ear bars. Meloxicam (5 mg/kg) (cat. # 6451603845, Henry Schein Animal Health) was administered subcutaneously in order to prevent inflammatory response. All surgical instruments were pre-sterilized. Using scissors that have been sterilized with ethanol, the skin over the top of the skull was removed starting with a horizontal cut all along the base of the head followed by two cuts in the rostral direction, almost reaching the eyelids, and then two oblique cuts that converge at the midline. A drop of 2% lidocaine solution (cat. # S1357, Selleckchem) was applied pre-emptively onto the periosteum to avoid any pain. With a scalpel, the periosteum was retracted to the edges of the skull. The musculature at the back of the neck was also slightly retracted. The animal was imaged with intact skull in the RSOM. To create the cranial window, first, a circle of about  $7 \times 7$  mm or less in diameter was “drawn” gently with a stereotactic drill. After slight drilling, 2% lidocaine solution was applied again onto the skull surface. The drilling was stopped when a very thin layer of bone was left. Under a drop of saline and taking advantage of the bone trabeculae - the spongy structure of the bone - the craniotomy is lifted away from the skull with very thin tip forceps. The saline is important because it helps lift up the skull and prevent bleeding of the dura. Gelfoam (cat. # NC9841478, Pfizer) that has been previously soaked in saline was applied to the dura mater, in order to stop any small bleeding that sometimes occurs when the skull is removed. With the open skull, the mouse was placed back onto the bed of the RSOM. Using a sterile cotton swap, any excess saline was removed, and a generous amount of clear ultrasound gel (cat. # 03-08, Parker Laboratories Inc.) was applied on top of the exposed brain. All mice were sacrificed shortly after imaging.

### **Vasoconstriction by epinephrine and endothelin-1.**

To investigate the sensitivity of our prototype RSOM scanner and to demonstrate that fast and temporal vascular changes can be monitored, we used the short-acting vasoconstrictors

epinephrine (L-Adrenaline, cat. # B1337, ApexBio) and endothelin-1 (cat. # E7764, Sigma-Aldrich). Shaved BALB/c mice with CT26 tumours, as described above, were used for this study (n = 3 for each vasoconstrictor). First, a tail vein catheter was inserted to enable rapid, consecutive image acquisition without removing the mouse from the RSOM scanner. The tumour was imaged before as well as 1 min, 5 min, and 10 min after injection of either 4 mg/kg epinephrine (in 10% DMSO (cat. # D2650, Sigma-Aldrich)) or 0.5 µg endothelin-1 (in 100 µL sodium chloride solution (cat. # BP358-1, Fisher Scientific)). As a comparison, the contralateral side of the mouse without tumour was imaged over the same period of time after vasoconstrictor injection. No laser illumination was applied for this experiment. MIP images were analysed by measuring the diameter of several representative vessels in tumours and skin over time by drawing a straight line from one side of the respective vessel to the other side using ImageJ (Fiji), and measuring the relative vessel diameter over time after vasoconstrictor injection in relation to the diameter before. Here, the vessel diameter correlates with the emitted ultrasound frequencies with smaller vessels emitting a range of higher frequencies and larger vessels emitting a range of lower frequencies as mentioned before.

### VTP with Padeliporfin.

Lyophilized palladium-bacteriochlorophyll derivative Padeliporfin (Tookad®-soluble, formulated as Padeliporfin di-potassium, also called WST11, Steba Biotech, France) was dissolved under light-protected conditions in sterile 5% dextran in water at 2 mg/mL and stored at -20 °C. Before VTP, an aliquot was thawed and filtered through a 0.2 mm syringe filter. CT26 tumour-bearing mice were first infused via tail vein with 9 mg/kg of Padeliporfin (not temperature-controlled) for 5 min and the tumour was immediately illuminated using a 753-nm diode laser (Modulight) for 10 min at 120 mW/cm<sup>2</sup> (corresponding to a total light dose of 72 J/cm<sup>2</sup>). During illumination, skin around the tumour was covered with a black sheet to prevent treatment response in healthy tissue. Animals were imaged using RSOM before VTP and at multiple time points afterwards for either short-term (5, 10, 30, and 60 min, n = 3) or long-term (1, 8, 18, 24, 30, 48 h, 3 d, 4 d, and 5 d, n = 3) monitoring of vascular changes. For the short-term imaging time points after VTP, the animals were kept in place for the entire time. For long-term imaging, the animals were removed after each scan from the RSOM and repositioned for each imaging session. For quantification, regions of interest were manually drawn on the MIP images using ImageJ, including only the tumour area but not the surrounding skin vessels. Longitudinal data were not co-registered but analysed separately. From RSOM images, the following parameters were analysed using ImageJ software: haemoglobin signal, total vascular area, and number of vessel fragments. The haemoglobin signal was calculated over time for each tumour by counting the pixels within the tumour area which were above a certain signal intensity, both, for smaller (green) and larger (red) vessels. Haemorrhage (diffuse signal in low frequencies) and clotted blood vessels (intense, dotted signal in both frequency ranges) were distinguished qualitatively within the images. The vascular area was also calculated within thresholded images and by measuring the area occupied by blood vessels within the tumour. Vessel fragments were quantified by counting the number of particles within thresholded RSOM images. No specific plugins were used. For all 3 parameters, the detected number before therapy was set to 100% and the following time points were calculated in

relation to before VTP. The same VTP treatment was performed for dual-wavelength RSOM imaging; oxygenation levels were determined before and at 5 min, 1 h, and 24 h after VTP. Controls, such as animals with Padeliporfin infusion or laser illumination only, were not included in this study as there are no expected changes of the tumour vessels as known from previous studies<sup>6,8,19</sup>.

### **Comparison of VTP impact in human patient-derived xenografts.**

RSOM imaging was used to examine the vascular response and neo-angiogenesis in tumour models that regressed or regrew after VTP. 5637 tumours (n = 11) and UMUC3 tumours (n = 11) were treated with VTP by retroorbital injection of 9 mg/kg Padeliporfin and 10 min of laser illumination at 150 mW/cm<sup>2</sup>, delivered at 5 min after drug injection. Tumours were imaged before treatment and at 1 h, 24 h, 3 d, 7 d, and 14 d after VTP and vascularization was analysed over time as described above (n = 3 per tumour model). Simultaneously, throughout the duration of the experiment, tumour volume was measured in both tumour models using a digital calliper (cat. # 1889–0600, Johnson) and the formula  $V = \frac{\pi}{6} \times (\text{length} \times \text{width} \times \text{height})$ . Tumour volume after therapy was compared to the volume before VTP to determine relative change over time.

### **Histological analysis.**

From mice euthanized at 24 h, 7 d, and 14 d, excised tumour tissues were fixed in 4% paraformaldehyde (cat. # 43368, Alfa Aesar) overnight at 4 °C or, if tumours reached a size >1 cm as in control mice, at room temperature to ensure complete fixation. Tissues were then washed 3 times in water and stored until further processing in 70% ethanol (cat. # 459836, Sigma-Aldrich). After embedding in paraffin (cat. # 39601006, Leica Biosystems), the tumours were cut into 10 µm slices and stained using Haematoxylin (cat. # 26381–02, Electron Microscopy Sciences) and Eosin (cat. # HT110216, Sigma-Aldrich) (H&E) for general tissue staining, antibody against CD31 (Dianova, cat. # DIA-310, 2µg/ml) for endothelial cells and thus blood vessels, and terminal deoxynucleotidyl transferase dUTP nick end labelling (TUNEL (cat. # 11093070910, Sigma-Aldrich)) to detect apoptotic cells. Staining was performed by the MSK Cytology Core facility following established protocols. The tissue slices were scanned with a high-resolution digital slide scanner (Pannoramic 250, 3DHistech).

### **Statistics.**

Data are indicated as mean values ± standard deviation (SD) or standard error of the mean (SEM) if not otherwise specified. Values were collected in Microsoft Excel and compared by unpaired two-tailed Student's *t* test using GraphPad Prism Version 6.01. A *p*-value of 0.05 or less was considered statistically significant.

### **Supplementary Material**

Refer to Web version on PubMed Central for supplementary material.

## Acknowledgements

This study was funded by the Thompson Family Foundation (Wade F. B. Thompson Grant to JC, AS and JG) and the National Cancer Institute (R01 CA212379 to JG). In part, the study was also supported by the European Grant INNODERM (687866) Horizon 2020. We acknowledge Dr. Pat Zanzonico and Valerie Ann Longo of the Small Animal Imaging Core Facility of MSKCC for their support (the Core is funded by the NIH Cancer Centre Support Grant P30 CA008748). We thank Ning Fan of MSKCC's Molecular Cytology Core Facility for assistance with histology, Yevgeniy Romin for support and feedback on image analysis, and Dmitry Yarilin of MSKCC's Molecular Cytology Core Facility for immunohistochemistry.

## References

1. Lin Z, Zhang Q & Luo W Angiogenesis inhibitors as therapeutic agents in cancer: Challenges and future directions. *European journal of pharmacology* 793, 76–81, doi:10.1016/j.ejphar.2016.10.039 (2016). [PubMed: 27840192]
2. Gunther JE et al. Dynamic Diffuse Optical Tomography for Monitoring Neoadjuvant Chemotherapy in Patients with Breast Cancer. *Radiology* 287, 778–786, doi:10.1148/radiol.2018161041 (2018). [PubMed: 29431574]
3. Madar-Balakirski N et al. Permanent occlusion of feeding arteries and draining veins in solid mouse tumors by vascular targeted photodynamic therapy (VTP) with Tookad. *PloS one* 5, e10282, doi:10.1371/journal.pone.0010282 (2010). [PubMed: 20421983]
4. Goldschmidt R, Vyacheslav K & Scherz A in *Optical Methods for Tumor Treatment and Detection: Mechanisms and Techniques in Photodynamic Therapy XXVI* (eds Kessel DH & Hasan T) (SPIE, 2017).
5. Gross S, Gilead A, Scherz A, Neeman M & Salomon Y Monitoring photodynamic therapy of solid tumors online by BOLD-contrast MRI. *Nature medicine* 9, 1327–1331, doi:10.1038/nm940 (2003).
6. Fleshker S, Preise D, Kalchenko V, Scherz A & Salomon Y Prompt assessment of WST11-VTP outcome using luciferase transfected tumors enables second treatment and increase in overall therapeutic rate. *Photochemistry and photobiology* 84, 1231–1237, doi:10.1111/j.1751-1097.2008.00340.x (2008). [PubMed: 18399928]
7. Cornelis FH et al. Contrast enhanced ultrasound imaging can predict vascular-targeted photodynamic therapy induced tumor necrosis in small animals. *Photodiagnosis and photodynamic therapy* 20, 165–168, doi:10.1016/j.pdpdt.2017.09.002 (2017). [PubMed: 28887222]
8. Neuschmelting V et al. WST11 Vascular Targeted Photodynamic Therapy Effect Monitoring by Multispectral Optoacoustic Tomography (MSOT) in Mice. *Theranostics* 8, 723–734, doi:10.7150/thno.20386 (2018). [PubMed: 29344301]
9. Johnson SP, Ogunlade O, Lythgoe MF, Beard P & Pedley RB Longitudinal photoacoustic imaging of the pharmacodynamic effect of vascular targeted therapy on tumors. *Clin Cancer Res*, doi:10.1158/1078-0432.CCR-19-0360 (2019).
10. Ntziachristos V & Razansky D Molecular imaging by means of multispectral optoacoustic tomography (MSOT). *Chemical reviews* 110, 2783–2794, doi:10.1021/cr9002566 (2010). [PubMed: 20387910]
11. Taruttis A & Ntziachristos V Advances in real-time multispectral optoacoustic imaging and its applications. *Nature Photonics* 9, 219–227, doi:10.1038/nphoton.2015.29 (2015).
12. Aguirre J et al. Precision assessment of label-free psoriasis biomarkers with ultra-broadband optoacoustic mesoscopy. *Nature Biomedical Engineering* 1, 1–8, doi:10.1038/s41551-017-0068 (2017).
13. Omar M, Schwarz M, Soliman D, Symvoulidis P & Ntziachristos V Pushing the optical imaging limits of cancer with multi-frequency-band raster-scan optoacoustic mesoscopy (RSOM). *Neoplasia* 17, 208–214, doi:10.1016/j.neo.2014.12.010 (2015). [PubMed: 25748240]
14. Omar M et al. Optical imaging of post-embryonic zebrafish using multi orientation raster scan optoacoustic mesoscopy. *Light: Science & Applications* 6, 1–6, doi:10.1038/lsa.2016.186 (2017).
15. Aguirre J et al. Broadband mesoscopic optoacoustic tomography reveals skin layers. *Optics letters* 39, 6297–6300, doi:10.1364/OL.39.006297 (2014). [PubMed: 25361338]



16. Schwarz M, Omar M, Buehler A, Aguirre J & Ntziachristos V Implications of ultrasound frequency in optoacoustic mesoscopy of the skin. *IEEE transactions on medical imaging* 34, 672–677, doi:10.1109/TMI.2014.2365239 (2015). [PubMed: 25361501]
17. Bereznoi A et al. Assessing hyperthermia-induced vasodilation in human skin in vivo using optoacoustic mesoscopy. *Journal of biophotonics*, e201700359, doi:10.1002/jbio.201700359 (2018). [PubMed: 29573174]
18. Schwarz M, Buehler A, Aguirre J & Ntziachristos V Three-dimensional multispectral optoacoustic mesoscopy reveals melanin and blood oxygenation in human skin in vivo. *Journal of biophotonics*, doi:10.1002/jbio.201500247 (2015).
19. Mazor O et al. WST11, a novel water-soluble bacteriochlorophyll derivative; cellular uptake, pharmacokinetics, biodistribution and vascular-targeted photodynamic activity using melanoma tumors as a model. *Photochemistry and photobiology* 81, 342–351, doi:10.1562/2004-06-14-RA-199 (2005). [PubMed: 15623318]
20. Brandis A et al. Novel water-soluble bacteriochlorophyll derivatives for vascular-targeted photodynamic therapy: synthesis, solubility, phototoxicity and the effect of serum proteins. *Photochemistry and photobiology* 81, 983–993, doi:10.1562/2004-12-01-RA-389 (2005). [PubMed: 15839743]
21. Azzouzi AR et al. TOOKAD(R) Soluble focal therapy: pooled analysis of three phase II studies assessing the minimally invasive ablation of localized prostate cancer. *World journal of urology* 33, 945–953, doi:10.1007/s00345-015-1505-8 (2015). [PubMed: 25712310]
22. Noweski A et al. Medium-term Follow-up of Vascular-targeted Photodynamic Therapy of Localized Prostate Cancer Using TOOKAD Soluble WST-11 (Phase II Trials). *European urology focus*, doi:10.1016/j.euf.2018.04.003 (2018).
23. Taneja SS et al. Final Results of a Phase I/II Multicenter Trial of WST11 Vascular Targeted Photodynamic Therapy for Hemi-Ablation of the Prostate in Men with Unilateral Low Risk Prostate Cancer Performed in the United States. *The Journal of urology* 196, 1096–1104, doi:10.1016/j.juro.2016.05.113 (2016). [PubMed: 27291652]
24. Ashur I et al. Photocatalytic generation of oxygen radicals by the water-soluble bacteriochlorophyll derivative WST11, noncovalently bound to serum albumin. *The journal of physical chemistry. A* 113, 8027–8037, doi:10.1021/jp900580e (2009). [PubMed: 19545111]
25. Durand RE Intermittent blood flow in solid tumours--an under-appreciated source of 'drug resistance'. *Cancer metastasis reviews* 20, 57–61 (2001). [PubMed: 11831648]
26. Morikawa S et al. Abnormalities in pericytes on blood vessels and endothelial sprouts in tumors. *The American journal of pathology* 160, 985–1000, doi:10.1016/S0002-9440(10)64920-6 (2002). [PubMed: 11891196]
27. Rahbari NN et al. Anti-VEGF therapy induces ECM remodeling and mechanical barriers to therapy in colorectal cancer liver metastases. *Science translational medicine* 8, 360ra135, doi:10.1126/scitranslmed.aaf5219 (2016).
28. Jain RK Antiangiogenesis strategies revisited: from starving tumors to alleviating hypoxia. *Cancer cell* 26, 605–622, doi:10.1016/j.ccell.2014.10.006 (2014). [PubMed: 25517747]
29. Hernandez-Agudo E et al. Monitoring vascular normalization induced by antiangiogenic treatment with (18)F-fluoromisonidazole-PET. *Molecular oncology* 10, 704–718, doi:10.1016/j.molonc.2015.12.011 (2016). [PubMed: 26778791]
30. Yang J et al. MR imaging biomarkers evaluating vascular normalization window after anti-vessel treatment. *Oncotarget* 9, 11964–11976, doi:10.18632/oncotarget.22600 (2018). [PubMed: 29552285]
31. Biel NM, Lee JA, Sorg BS & Siemann DW Limitations of the dorsal skinfold window chamber model in evaluating anti-angiogenic therapy during early phase of angiogenesis. *Vascular cell* 6, 17, doi:10.1186/2045-824X-6-17 (2014). [PubMed: 25101168]
32. Kimm SY et al. Nonthermal Ablation by Using Intravascular Oxygen Radical Generation with WST11: Dynamic Tissue Effects and Implications for Focal Therapy. *Radiology* 281, 109–118, doi:10.1148/radiol.2016141571 (2016). [PubMed: 26986047]

33. Mallidi S, Watanabe K, Timerman D, Schoenfeld D & Hasan T Prediction of tumor recurrence and therapy monitoring using ultrasound-guided photoacoustic imaging. *Theranostics* 5, 289–301, doi:10.7150/thno.10155 (2015). [PubMed: 25553116]
34. Wang HW et al. Treatment-induced changes in tumor oxygenation predict photodynamic therapy outcome. *Cancer research* 64, 7553–7561, doi:10.1158/0008-5472.CAN-03-3632 (2004). [PubMed: 15492282]
35. Jathoul AP et al. Deep in vivo photoacoustic imaging of mammalian tissues using a tyrosinase-based genetic reporter. *Nature Photonics* 9, 239–246, doi:10.1038/nphoton.2015.22 (2015).
36. He H et al. Capsule Optoacoustic Endoscopy for Esophageal Imaging. *Journal of biophotonics*, doi:10.1002/jbio.201800439 (2019).
37. Haedicke K et al. Sonophore labeled RGD: a targeted contrast agent for optoacoustic imaging. *Photoacoustics* 6, 1–8, doi:10.1016/j.pacs.2017.03.001 (2017). [PubMed: 28393018]
38. Caballero MAA Incorporating Sensor Properties in Optoacoustic Imaging Ph.D. thesis, Technical University Munich, (2013).

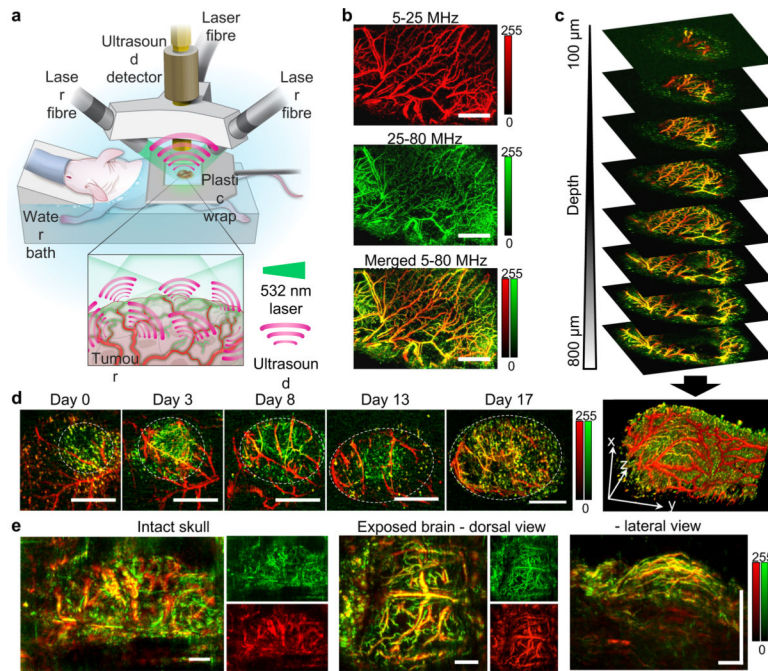


**Figure 1. RSOM imaging of CT26 colon carcinoma tumours and mouse brain.**

**a**, Schematic illustration of the experimental setup for RSOM scanning of a mouse with a subcutaneous tumour. The animal is positioned in a water bath to couple the transducer to the animal. The 3 laser fibres coupled rigidly to the ultrasound detector scan in a raster pattern over the assigned field of view, which is stabilized using a thin foil. After nanosecond-pulsed laser illumination at 532 nm, ultrasound waves are detected immediately.

**b**, Optoacoustic MIP images of a CT26 tumour. Detected ultrasound frequencies were divided into two sub-bands to represent bigger (5–25 MHz, depicted in red) and smaller (25–80 MHz, shown in green) blood vessels. Yellow colours represent merging of both frequency bands. Scale bar = 4 mm. **c**, MIP images of slices through a CT26 tumour up to 800 µm depth. Each image represents a 100 µm slice. Below, 3D reconstruction of a CT26 tumour viewed from within the animal towards the skin.

**d**, CT26 tumour growth over 17 days after implantation. Red, 5–25 MHz (larger vessels); green, 25–80 MHz (smaller vessels); yellow, merge/overlap of high and low frequency signals (scale bar applies to all images in this work unless specified otherwise); white circle, tumour area. Scale bar = 4 mm.

**e**, RSOM MIP images of an intact mouse skull (image shows half of the skull with skin removed) and an exposed brain after removing the skullcap in dorsal and lateral view. Scale bar = 1 mm. Major vessels can still be identified on the right side of the brain through the skull bone.

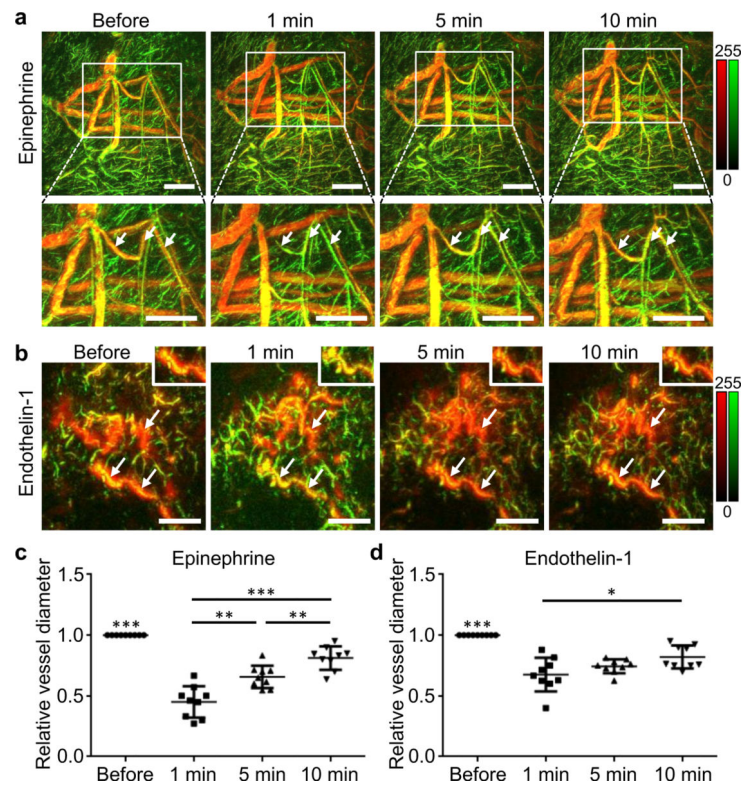


**Figure 2. RSOM imaging of pharmacologic vasoconstriction in CT26 tumours after injection of epinephrine or endothelin-1.**

**a**, MIP images of CT26 tumour vessels over the 10 min after injection of epinephrine. Arrows in enlarged images indicate vasoconstriction. Scale bar = 2 mm. **b**, MIP images of CT26 tumour vessels over the 10 min after injection of endothelin-1. Small inserts show changes in a single blood vessel over time. Scale bar = 1 mm. **c-d**, Relative vessel diameters from 3 different tumours ( $n = 3$ , biological replicates) over the 10 min after epinephrine (**c**) or endothelin-1 (**d**) injection. Mean  $\pm$  SD of 3 mice. Data were compared using unpaired two-tailed Student's *t* test. \*\*\*  $P < 0.0001$ , \*\*  $P = 0.0013$  for 1 min vs. 5 min, and 0.0031 for 5 min vs. 10 min, \*  $P = 0.0195$ .

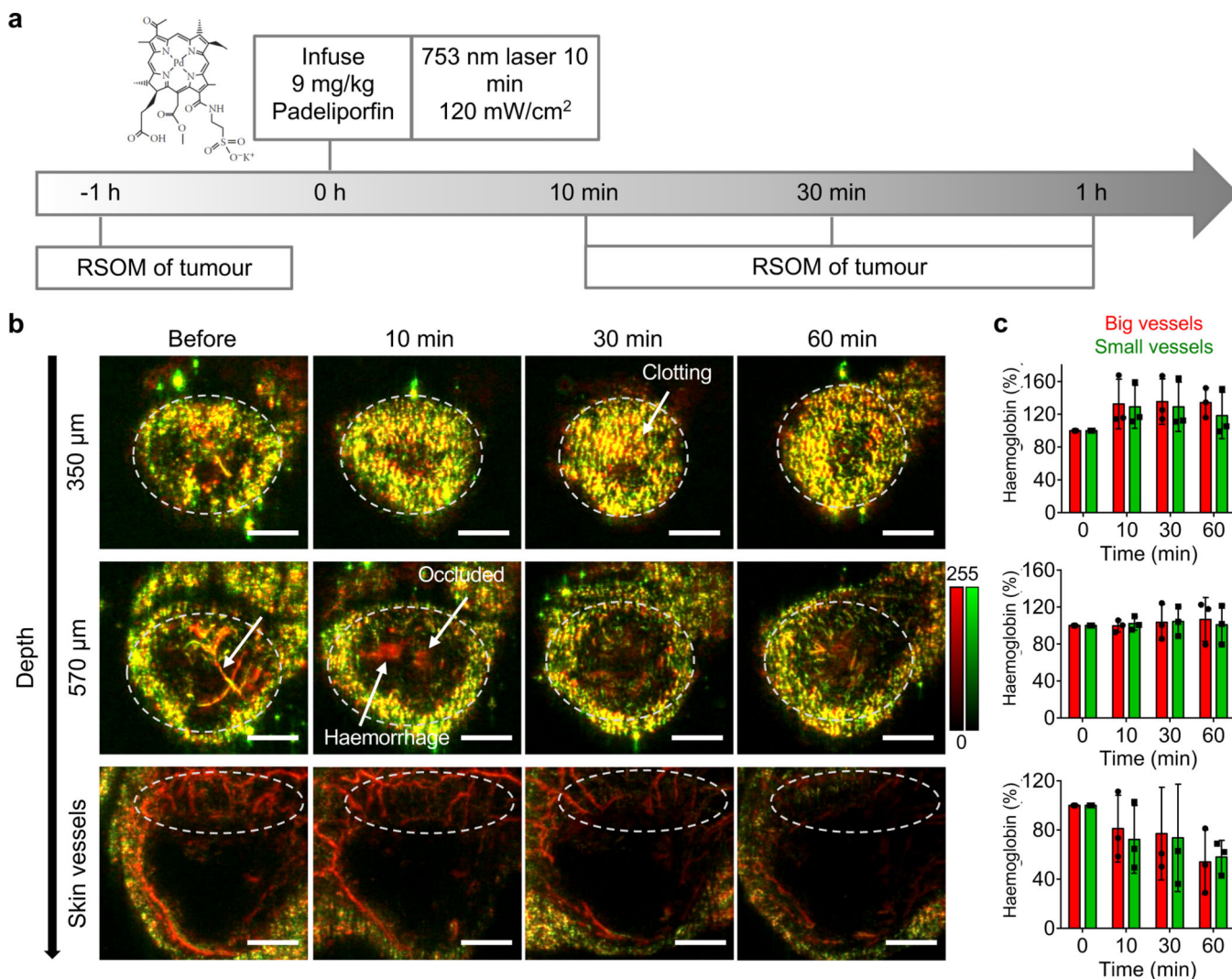


**Figure 3. RSOM imaging of Padeliporfin VTP in CT26 tumours and skin vessels over time.** **a**, Schematic of Padeliporfin VTP, including photosensitizer infusion, laser illumination, and RSOM imaging at multiple time points. Chemical structure of the palladium-bacteriochlorophyll derivative Padeliporfin. **b**, RSOM images (single slices) of a CT26 tumour at varying depths (350 µm, 570 µm, skin level) before and over time after VTP. Dotted circles delineate the tumour or skin area analysed in **c**. Arrows indicate clotted and occluded vessels and VTP-induced haemorrhage. Scale bar = 2 mm. **c**, Quantitative analysis of the relative amount of haemoglobin in tumour and skin vessels in the red (larger vessels) and green (smaller vessels) channels over time up to 60 min after VTP.  $n = 3$ , biological replicates. Mean  $\pm$  SD.

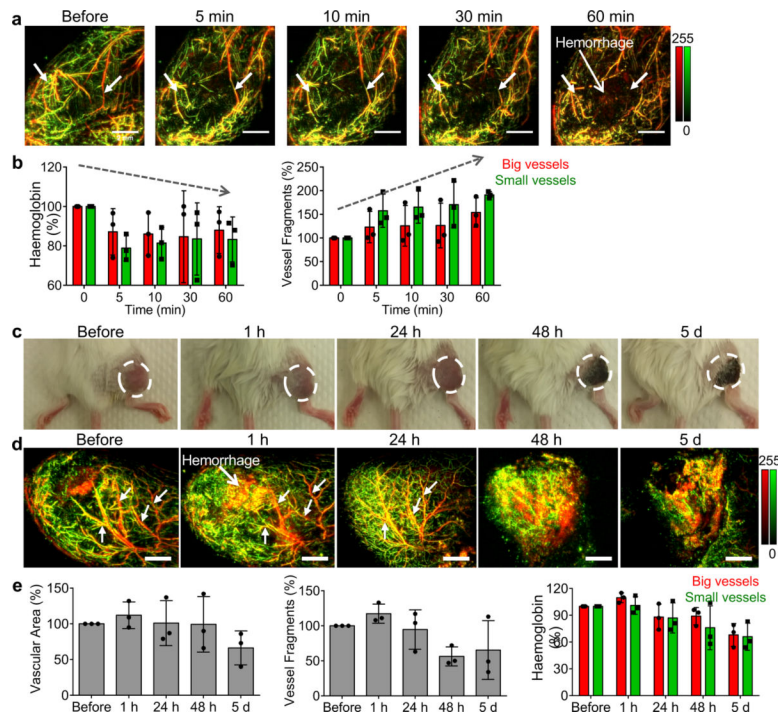


**Figure 4. Short- and long-term longitudinal RSOM imaging of Padeliporfin VTP effects in CT26 tumours.**

**a**, RSOM MIP images of a CT26 tumour after Padeliporfin VTP over time. Arrows indicate the destruction of representative vessels and haemorrhage after 60 min. Scale bar = 2 mm. **b**, Quantitative analysis of VTP effect. Relative amount of haemoglobin and the number of vessel fragments were quantified in each frequency channel over time.  $n = 3$ , biological replicates. Mean  $\pm$  SD. **c**, Photographs of a BalbC mouse with CT26 tumour in the right thigh over time up to 5 days after VTP treatment. Dark tissue reflects necrosis. Dotted circle = tumour area. **d**, RSOM MIP images of the vascular network of a CT26 tumour over time up to 5 days after Padeliporfin VTP. Arrows follow individual vessels over time. Scale bar = 2 mm. **e**, Quantitative analysis of the relative vascular area (total signal), relative number of vessel fragments, and relative haemoglobin signal in the red (larger vessels) and green (smaller) channels in CT26 tumours after VTP over time.  $n = 3$ , biological replicates. Mean  $\pm$  SD.

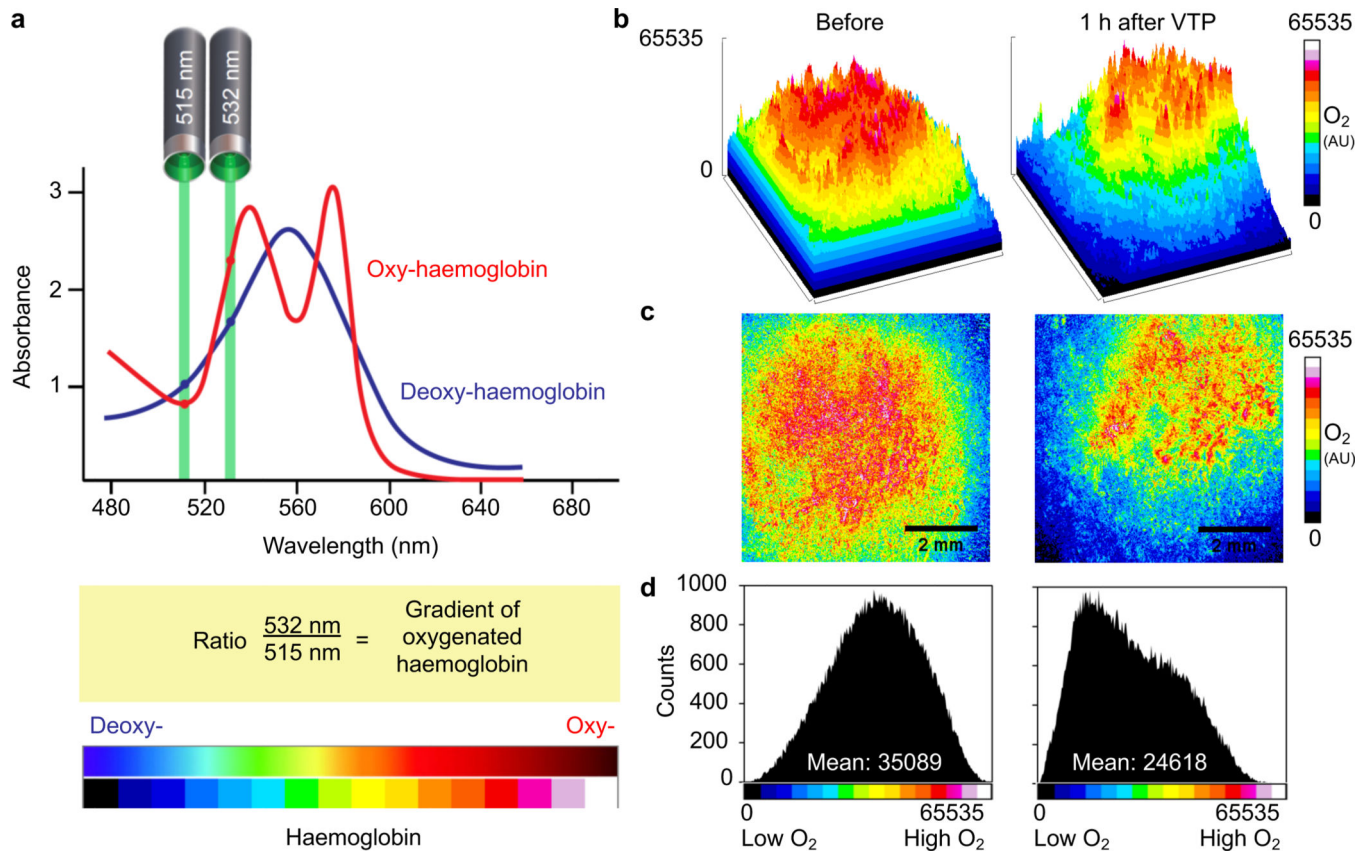


**Figure 5. Dual-wavelength RSOM imaging before and 1 h after Padeliporfin VTP to visualize tumour oxygenation.**

**a**, Absorbance spectra of oxy- (red) and deoxyhaemoglobin (blue). The green laser beams mark the wavelengths used for dual-wavelength RSOM imaging. The ratio of the signal at 532 nm to 515 nm was used to calculate the gradient of oxygenated haemoglobin. Scales below illustrate the colour scheme used in the oxygenation images (black/blue, low oxygen; red/white, high oxygen). **b**, 3D surface plots of oxygenation before and 1 h after VTP. Axis = 6.8 mm. **c**, Dual-wavelength RSOM MIP images of relative tumour oxygenation before and 1 h after therapy. Scale bar = 2 mm. **d**, Histogram of the distribution of the oxygenation values before and 1 h after VTP.

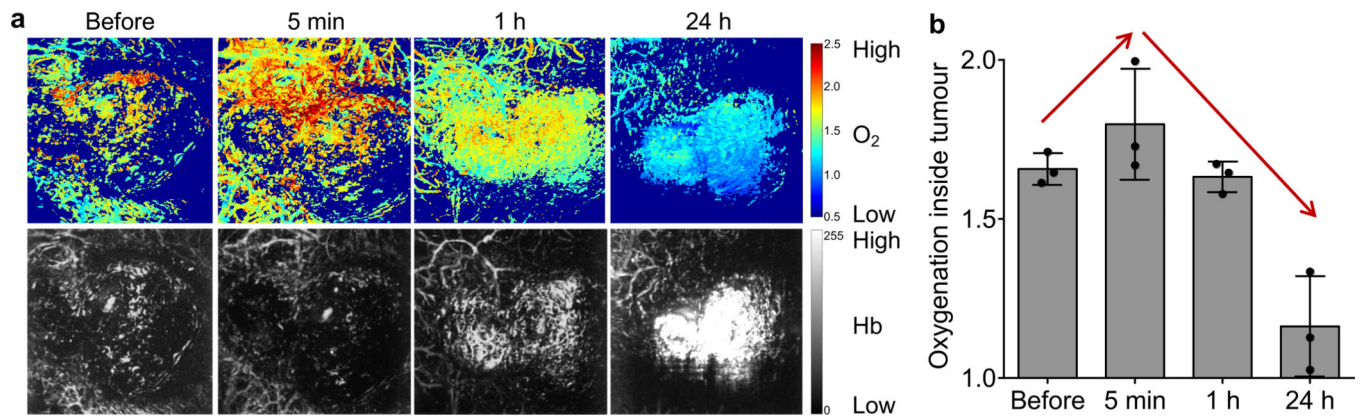


**Figure 6. Dual-wavelength RSOM imaging of tumour oxygenation and vascularization in CT26 tumours over time after Padeliporfin VTP.**

**a**, Dual-wavelength RSOM MIP images of relative oxygenation levels in a CT26 tumour up to 24 h after Padeliporfin VTP. Blue = low oxygen. Red = high oxygen. Lower grey-scale images show corresponding RSOM MIPs of the tumour vasculature over time. **b**, Quantitative analysis of relative oxygenation in tumours over time after VTP. Red arrows show the trend of oxygenation changes over time. n = 3, biological replicates. Mean ± SD.



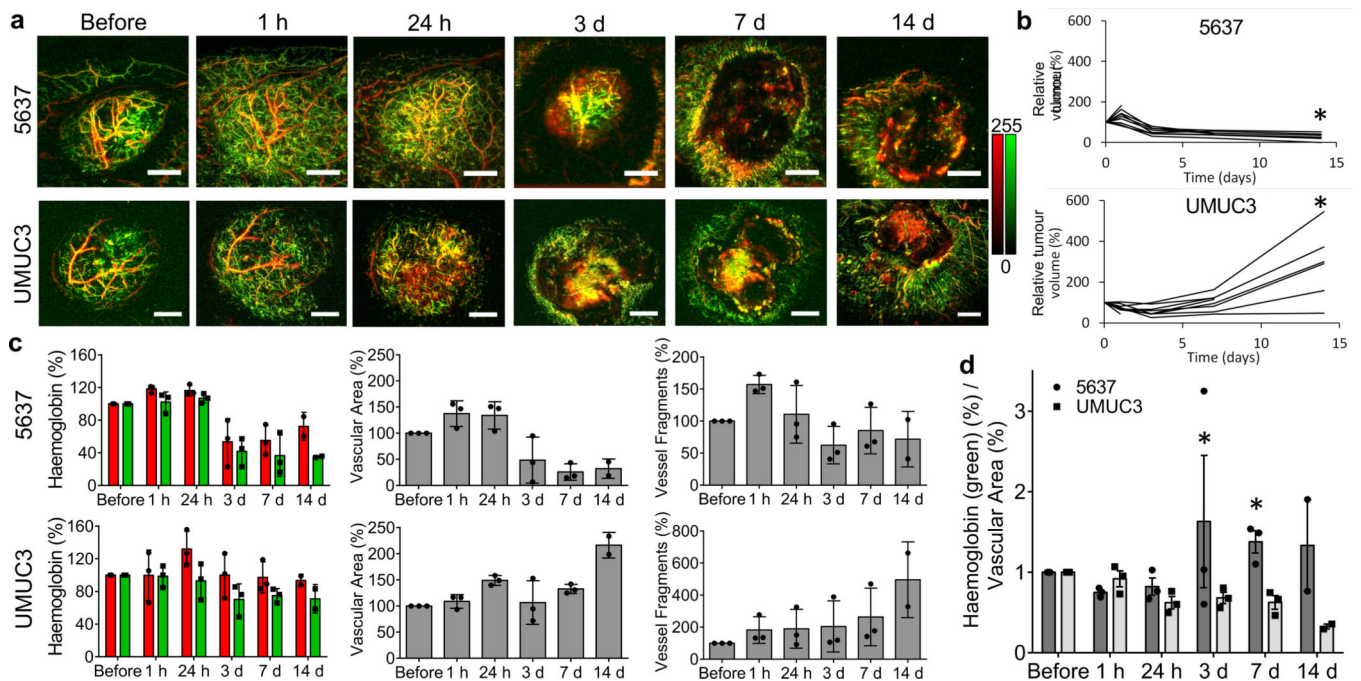


**Figure 7. Comparison of vascularization between bladder tumours in which VTP is differentially effective.**

**a**, RSOM MIP images of the vasculature of 5637 and UMUC3 tumours over time up to 14 days after Padeliporfin VTP. Scale bar = 2 mm. **b**, Relative tumour volume of 5637 and UMUC3 tumours over time after VTP. \*  $P$  at 14 days = 0.0114. **c**, Quantification of relative haemoglobin levels in the low-frequency (red) and high-frequency (green) channels, relative vascular area, and relative number of vessel fragments in 5637 and UMUC3 tumours after VTP over time.  $n = 3$ ,  $n = 2$  for 14 days, biological replicates. Mean  $\pm$  SD. **d**, Ratio of normalized haemoglobin (%) in the high-frequency (green) channel to normalized vascular area (%) in 5637 and UMUC3 tumours over time after VTP.  $n = 3$ ,  $n = 2$  for 14 days, biological replicates. Mean  $\pm$  SEM. Data were compared using unpaired two-tailed Student's  $t$  test. \*  $P = 0,0239$  for 3 days, and 0.0096 for 7 days (adjusted  $p$ -value).

**Table 1:**

Biological interpretation of the RSOM image features.

<b>RSOM image feature</b>	<b>Biological interpretation</b>
Connected network of homogenous signals	Blood vessels in tumour and skin
Green-coded vascular structures	High ultrasound frequencies (25–80 MHz) denotating smaller blood vessels with ~15–48 $\mu\text{m}$ diameter <sup>1</sup>
Red-coded vascular structures	Low ultrasound frequencies (5–25 MHz) denotating larger blood vessels with ~48–240 $\mu\text{m}$ diameter <sup>2</sup>
Dotted yellow-coded structures	Clotted blood emitting a wide range of ultrasound frequencies of 5–80 MHz
Loss of signal over time to no signal	Occluded or destructed blood vessels
Homogenous red-coded signal of larger extend, not adhering to vascular structures	Haemorrhage into the tumour tissue from disrupted blood vessels
Extended area of irregular signal intensity without vascular structures	Necrotic tissue

<sup>1</sup> refers mainly to capillaries and capillary-like vessels

<sup>2</sup> refers mainly to feeding arteries / arterioles as well as draining veins / venules